

Journal of Materials Chemistry A

Accepted Manuscript



This article can be cited before page numbers have been issued, to do this please use: C. Huang and P. Grant, *J. Mater. Chem. A*, 2018, DOI: 10.1039/C8TA05049J.



This is an Accepted Manuscript, which has been through the Royal Society of Chemistry peer review process and has been accepted for publication.

Accepted Manuscripts are published online shortly after acceptance, before technical editing, formatting and proof reading. Using this free service, authors can make their results available to the community, in citable form, before we publish the edited article. We will replace this Accepted Manuscript with the edited and formatted Advance Article as soon as it is available.

You can find more information about Accepted Manuscripts in the [author guidelines](#).

Please note that technical editing may introduce minor changes to the text and/or graphics, which may alter content. The journal's standard [Terms & Conditions](#) and the ethical guidelines, outlined in our [author and reviewer resource centre](#), still apply. In no event shall the Royal Society of Chemistry be held responsible for any errors or omissions in this Accepted Manuscript or any consequences arising from the use of any information it contains.

Coral-like directional porosity lithium ion battery cathodes by ice templating

Chun Huang and Patrick S. Grant*

Dr. Chun Huang, Prof. Patrick S. Grant

Department of Materials, University of Oxford, Oxford, OX1 3PH, United Kingdom

E-mail: ann.huang@materials.ox.ac.uk

Abstract

Thick electrodes ($>500\ \mu\text{m}$) that minimize the proportion of inactive components (current collectors, separators, etc.) are attractive for high energy density lithium ion battery (LIB) cell-stacks. However, the tortuous porosity inside the electrodes usually restricts the use of these more cost-effective thick electrodes, because lithium ion diffusion becomes restricted and capacity reduces to impractical levels. To overcome this problem, we manufacture $900\ \mu\text{m}$ thick cathodes with aligned pore arrays in the predominant ion transport direction using a scalable ice templating technique without the need for post-processing sintering. The aligned porosity combined with a coral-like electrode structure exhibited high areal and gravimetric capacities ($14\ \text{mAh cm}^{-2}$ and $142\ \text{mAh g}^{-1}$ at $0.1\ \text{C}$) as well as a sustained rate capability at faster (dis)charge rates (e.g. $12\ \text{mAh cm}^{-2}$ and $124\ \text{mAh g}^{-1}$ at $1\ \text{C}$) that outperformed the capacities ($0.5\ \text{mAh cm}^{-2}$ and $141\ \text{mAh g}^{-1}$ at $0.1\ \text{C}$) and rate capability (e.g. $0.4\ \text{mAh cm}^{-2}$ and $103\ \text{mAh g}^{-1}$ at $1\ \text{C}$) of conventional LIB electrodes containing the same materials and with a random

microstructure fabricated by standard slurry casting. X-ray tomography and numerical modelling were used to quantify and confirm the aligned porosity benefits, which were preserved after many cycles of operation, along with robust mechanical integrity of the electrodes.

Introduction

Lithium ion battery (LIB) development is essential for applications in mobile devices, wide adoption of emission-free electric vehicles and megawatt-scale grid energy storage from intermittent renewable sources. LIB research and development have thus focused on maximizing energy density within a defined volume of LIB cell-stacks while maintaining high power density and long lifetime [1]. A conventional LIB cell consists of a cathode and an anode (20-100 μm) on metallic current collector foils that sandwich an electrically insulating but ion permeable separator, all of which are then immersed in a lithium ion containing liquid electrolyte [2–4]. During charging, lithium ions move from cathode to anode, and the process is reversed during discharging. This layer sequence is repeated to form a stack of LIB cells to achieve the required total stored energy [1].

The electrodes are usually made by a highly scalable slurry casting (SC) process involving doctor-blade coating of a mixed slurry onto a metallic current collector foil followed by drying, resulting in a random structure of four mixed phases that comprise the electrode: an active particulate material for reversible lithium insertion and extraction, an electrical conductivity enhancer, a binder to hold the particles together, and a random, tortuous pore network [5]. The maximum capacity of the electrode at a (dis)charge rate may be realized if all of the active material has a sufficient local supply of lithium ions and sufficient time for charge storage reactions to occur. In practice, restricted lithium ion diffu-

sion inside the microscopic, tortuous pore network of the electrodes made by SC limits the capacity at progressively faster and faster (dis)charge rates [6–9]. The most common method of improving rate capability (*i.e.* sustaining capacity retention with increasing (dis)charge rates) is to reduce electrode thickness to shorten the lithium ion diffusion pathway length between the two electrodes. However, reducing the electrode thickness leads to an increased proportion of inactive components such as current collectors and separators in an LIB cells stack and so reduces the energy density per stack. Although many studies have focused on developing new electrode materials to increase capacity by the ubiquitous SC process [10], the equally efficient strategy of optimizing performance via electrode microstructure engineering attracted less attention [11].

In order to increase flexibility in this energy-rate capability balance, novel nanostructures [12–22] and low pore-tortuosity electrode structures have been explored to improve ion diffusion kinetics without resorting to unrealistically thin electrodes [23]. These approaches include repeated co-extrusion and assembly of LiCoO_2 (LCO) cathode [24], magnetic templating of LCO cathode [2], infiltration and carbonization of natural wood frameworks to make LCO cathode [11] and LiFePO_4 cathode [25], and ice templating (also called freeze casting) of $\text{LiNi}_{0.8}\text{Co}_{0.15}\text{Al}_{0.05}\text{O}_2$ cathode [26], all of which showed a significant improvement in areal capacity and rate capability over conventional electrode structures. All of the methods above did not need/avoided any calendaring or pressing of the electrodes. Among these fabrication methods, ice templating was initially invented for making ceramic supports [27], but has recently also been investigated for making electrodes [26]. However, ice templating in previous studies, and the other fabrication methods mentioned above, all required sintering of cathodes at 600 to 2500 °C to remove the templates and provide mechanical stability of the powder-based electrode structures. Unfortunately, the need for sintering may eliminate some of the useful fine-scale (down to the nano-scale) inter-connected electrode porosity and reduce electrode/electrolyte interfacial area in

the densified electrodes, and so inhibiting overall capacity [26, 28, 29].

Lithium ion diffusion on the scale of an electrode is mainly governed by porosity fraction and pore tortuosity. Porosity fraction ε determines the amount of electrolyte and thus the lithium ions available for diffusive transport, while pore tortuosity τ expresses the restriction of lithium ion diffusion resulting from geometric convolutions of the ion flux paths [6, 30]. The most common method of correlating electrode porosity fraction with pore tortuosity is Bruggeman's correlation $\tau = \varepsilon^{-\alpha}$ where α is a constant ranging from 0.5 to 4 for the electrodes made by standard SC [6, 31]. However, Bruggeman's correlation assumes uniform, isotropic pore geometries with a random electrode structure [30]. Once deliberately aligned anisotropic porosity and the corresponding directional diffusion are considered, other characterization approaches are required [32, 33].

In this work, we design and fabricate an ultra-thick (900 μm) LCO cathode with a coral-like structure containing aligned pores in the through electrode thickness direction (the kinetically favorable lithium ion transport direction during charge and discharge) by directional ice templating (DIT). LCO is one of the most attractive materials to make ultra-thick cathodes due to its relatively high compaction density, moderate electronic conductivity and good cycling stability [11]. LCO was chosen here only as an exemplar, and DIT is likely essentially material-independent. The electrodes made by ice templating exhibited repeatable and sufficient mechanical strength for direct assembly into cells, along with excellent stability during cycling, *without* the need for post-processing sintering. The electrodes provide high areal and gravimetric capacities of 14.0, 12.2 and 8.3 mAh cm^{-2} (corresponding to 142.2, 123.9 and 84.1 mAh g^{-1}) at 0.1, 1 and 5 C respectively, providing an attractive combination of high capacity and rate capability. The areal capacities can be further increased through increasing electrode thickness without ion transport restrictions in the aligned porosity electrode. Compared with electrodes fabricated under

otherwise identical conditions by isotropic ice templating (IIT, uniform freezing from all directions) and conventional SC, all containing the same materials and random mixtures of the constituent phases, we show that in the same total volume including current collectors and separators, an LIB cell containing the ultra-thick, aligned porosity DIT electrode may exhibit 57% higher gravimetric energy density at 2 C than an LIB cell-stack containing the standard, higher density SC electrodes. We quantify the designed directional tortuosity by X-ray computed tomography (XCT) and numerical simulation to show that the highest performance of the DIT electrode could be attributed to fast lithium ion diffusion kinetics along the aligned pores at the micro-scale and facile lithium ion intercalation across the electrode/electrolyte interface at the nano-scale. Although operated only at laboratory scale here, ice templating offers reasonable prospects to be scaled to dimensions relevant for commercial battery production, with a rough estimate showing the possibility for a similar cost.

Results and discussion

Fabrication of electrodes by directional ice templating

Figure 1(a) is a schematic of the in-house DIT apparatus. A homogeneously mixed, aqueous suspension containing active LCO particles, electrically conducting carbon black nanoparticles, and a sodium carboxymethyl cellulose (CMC) binder at a weight ratio of 25 : 1 : 1 was directionally and rapidly frozen by contacting with a Cu cold finger, one end of which was immersed in liquid nitrogen. CMC dissociates to carry anionic charges in aqueous suspensions that provide electrostatic stabilization on the LCO particles [34, 35]. The freezing rate was measured at 0.1 K s^{-1} by thermocouples inserted at various locations in the mould close to the freezing surface.

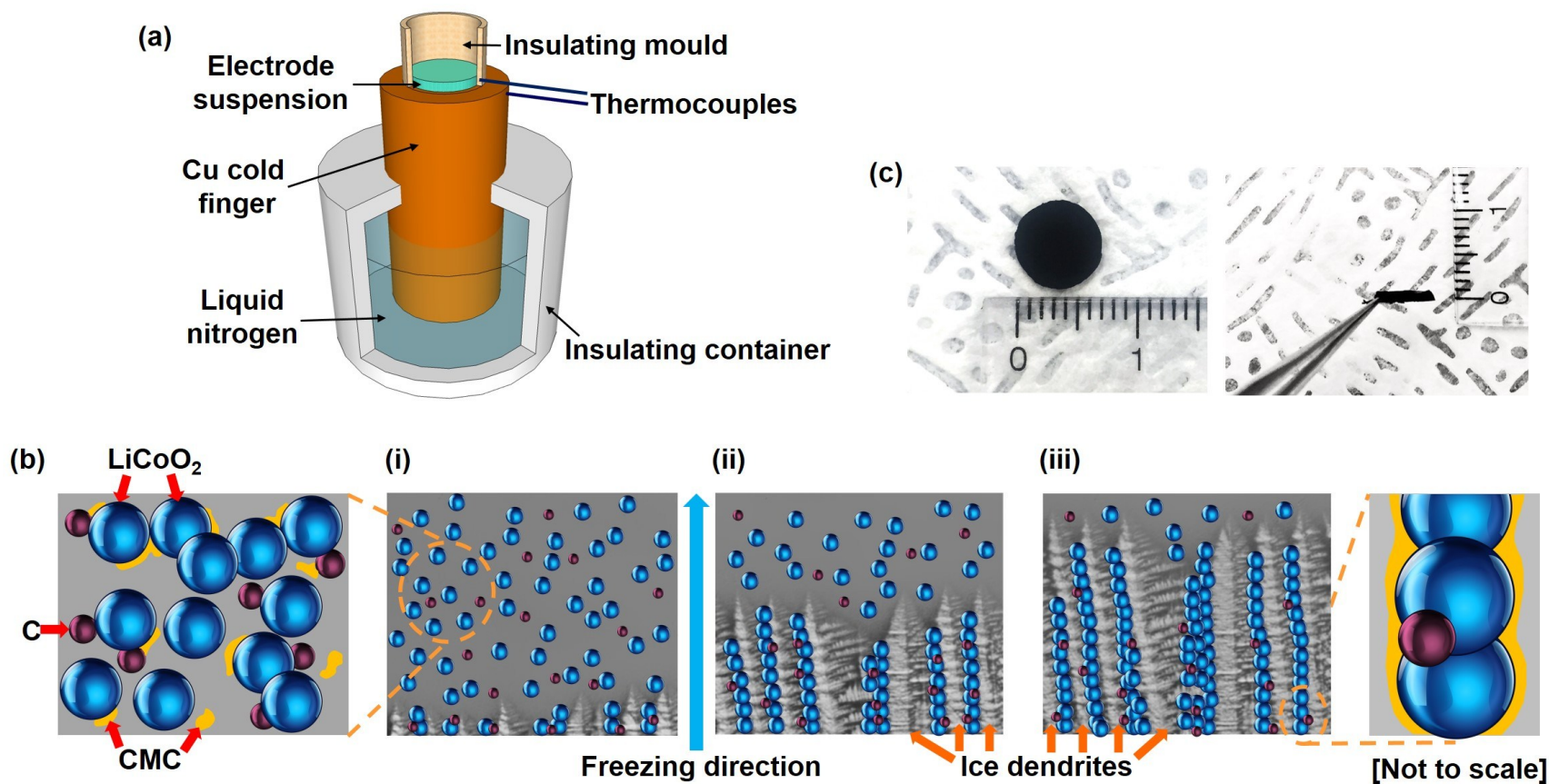


Figure 1: Schematics of the (a) DIT apparatus; and (b) DIT process. (c) Photos of a free-standing LCO electrode made by DIT.

Figure 1(b) is a schematic showing the mechanism of structural alignment by DIT. The stable aqueous suspension comprises the LCO particles and the carbon black nanoparticulates; a fraction of binder is dissolved in the water and the remainder adsorbed on the surface of the LCO and carbon black particles [36]. First in (i), ice crystals are nucleated on the surface of the Cu cold finger. In (ii), arrays of primary ice dendrites grow predominantly aligned to the steep 1D temperature gradient imposed by the cold finger, with smaller secondary ice dendrites branching side-ways. As freezing progresses, the liquid fraction reduces and the dispersed LCO and carbon black particles are pushed by the moving ice fronts into the channels between the ice dendrites, where their mean separation progressively decreases as water crystallizes and the local concentration of solid particles progressively increases. In the final step (iii), recognizing the slight volume expansion of water on freezing, particles trapped in the now interlocking “forest” of ice dendrites become subject to a small compressive force, overcoming any repulsive electrostatic force. As the last of the water freezes, the residual binder is precipitated over the LCO and carbon black particles [37]. After careful optimization of the suspension composition, the strength of the resulting free-standing green body was sufficient to allow robust manual handling and then ice sublimation under vacuum, without the need for any post-processing sintering [36,38]. Indeed, the self-standing electrodes were robust enough for gentle surface grinding and polishing by hand on abrasive SiC papers to ensure a consistent thickness; electrodes were then assembled into cells in a glovebox for testing. Supplementary Video 1 shows the electrode freezing process during DIT and the emergence of growing ice crystals from the electrode surface.

Figure 1(c) shows images of a free-standing DIT electrode and Figure S1 in the Supplementary Information (SI) shows the same electrode after cycling, further demonstrating mechanical stability. For comparison, similar LCO electrodes were also fabricated by IIT and SC, using the same suspension formulation. It was impossible to slurry cast electrodes of the same thickness as the ice templated

electrodes without cracking or delamination from the current collectors [25, 39], because such thick SC electrodes were unable to sustain the high internal strains and stresses accumulated by the capillary forces during electrode drying and solvent evaporation [4, 40]. Thus, 26 μm thick electrodes using the same electrode suspension were prepared. On the other hand, ice templating overcame the conventional SC electrode thickness restrictions, because the frozen water was directly sublimed from solid to gas, and thus avoiding strong capillary forces in conventional liquid-vapour drying [41]. The mass loading of the DIT, IIT and SC electrodes was 98.5, 110.2 and 3.5 $\text{mg cm}^{-2} \pm 4\%$ among 50 samples made by each type of fabrication method respectively. The surface status of the DIT, IIT and SC electrodes was the same. Performance among the DIT, IIT and thin SC electrodes (using the same electrode suspension) as well as the commercial SC electrodes is compared later.

Morphology and mechanical properties

Figures 2(a) and (b) are cross-sectional scanning electron microscopy (SEM) images of the IIT electrode. The primary LCO particles were 25 to 120 nm in size, with agglomeration into secondary particles of 0.8 to 3.2 μm . The pore width was 1.2 to 7.5 μm and randomly distributed. Due to nucleation of ice crystals throughout the electrode during IIT and in the absence of a strong temperature gradient, equiaxed ice crystal growth was soon restricted by neighbouring ice crystals (impingement) from all directions, resulting in pores that had no long range preferred orientation after ice sublimation.

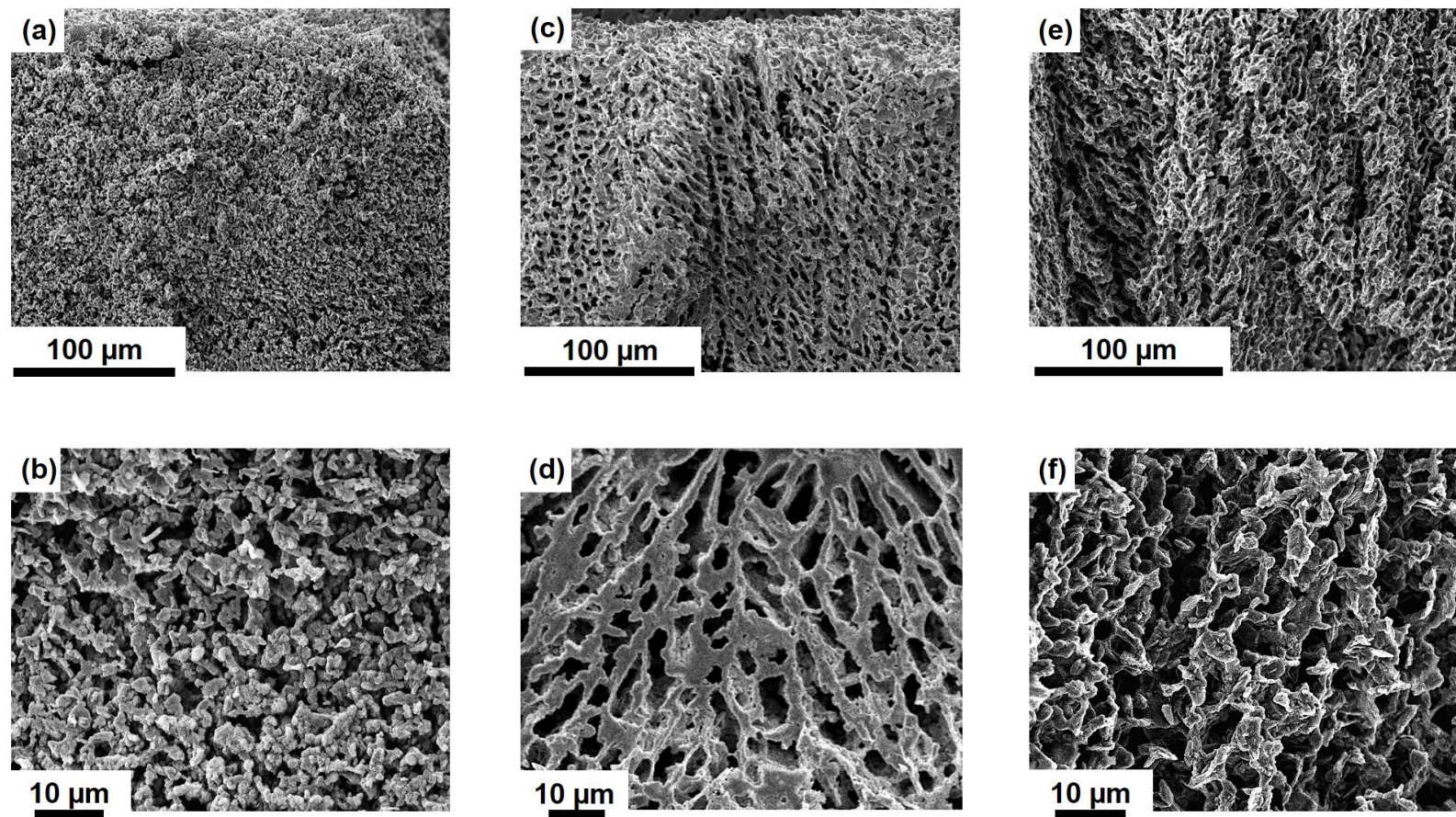


Figure 2: Cross sectional SEM images of (a) and (b) an electrode structure made by IIT; (c) and (d) an electrode structure made by DIT; (e) and (f) the electrode in (c) and (d) after 200 charge and discharge cycles.

Figures 2(c) and (d) are cross-sectional SEM images of the DIT electrode with identical composition. Particle agglomerates were now more compacted and discrete particle boundaries less obvious, suggesting more effective compressive forces on the particles during DIT [37]. The composite component of the DIT electrode had a coral-like structure with qualitatively greater pore inter-connectivity than the IIT electrode (pore structure quantified later). The primary pore “trunks” were aligned approximately in the through electrode thickness direction, sometimes extending beyond the field of view, with a micro-pore width of 5.5 to 7.3 μm and secondary pore widths of 790 nm to 3.5 μm . Figures 2(e) and (f) are the cross-sectional SEM images of the same DIT electrode after 200 (dis)charge cycles (described later), demonstrating excellent mechanical stability, with no evidence of pulverisation or large scale fracture. Figure S2 in the SI shows the X-ray diffraction (XRD) patterns of the DIT electrode before and after 200 cycles of charge and discharge. All the diffraction peaks in the XRD patterns corresponded to LiCoO_2 (PDF card no. 00-044-0145), confirming structural stability of the active material [42].

To investigate the effects of pore anisotropy on electrode mechanical response, compression tests were performed on the self-standing DIT and IIT electrodes. Figure S3 in the SI shows a schematic of the testing jig that applied a compressive force in the through thickness z direction, normal to the electrode polished surface. Figure S4(a) in the SI shows the resulting compressive stress-strain curves, and Figure S4(b) shows a magnified view at strains below 0.03%. The DIT electrode exhibited 3 times higher compression strength than the IIT electrode, because the DIT structure was a more efficient load carrying arrangement with near-parallel orientation of the composite “pillars” with respect to the direction of the applied uniaxial compressive load [27, 43–46]. The DIT electrode exhibited sufficient mechanical strength to be assembled into a swagelok cell under pressure. Electrical conductivity of the self-standing DIT electrodes was measured in a standard four-point probe configuration, following a method reported previously [47]. The average electrical conductivity of the DIT electrodes was 3.0 S

m^{-1} .

To investigate the effect of freezing rate on the electrode microstructure, a faster freezing rate of 0.5 K s^{-1} was investigated. Figures S5(a) and (b) in the SI show a cross-sectional SEM image and a 3D rendering of the resulting LCO electrode by XCT. The pore structure became more disordered and less aligned because a higher rate of ice crystal nucleation predominated over directional growth of the existing crystals. To investigate broader applicability of the DIT method, another cathode material $\text{LiNi}_{0.8}\text{Co}_{0.15}\text{Al}_{0.05}\text{O}_2$ (NCA) was also used for making thick ($900 \mu\text{m}$) electrode by DIT at a freezing rate of 0.1 K s^{-1} . Figures S6(a) and (b) in SI show a 3D rendering and a 2D cross-section rendering of the resulting NCA electrode by XCT, again showing a structure containing aligned pore arrays. Previous work on NCA electrodes made by ice templating reported a capacity of 13.3 and 8.3 mAh cm^{-2} at 0.1 and 0.2 C respectively [48].

Directional tortuosity and lithium ion diffusion simulation

Porosity and tortuosity are commonly measured by high pressure fluid intrusion e.g. mercury porosimetry, but this method only provides an estimation of isotropic tortuosity [49]. Here, porosity in 3D and directional tortuosity through the electrode thickness (the predominant lithium ion transport direction) were instead quantified by XCT. X-ray microtomograph grey-scale raw image data (voxel size of $200 \times 200 \times 200 \text{ nm}$) from the electrodes was threshold divided into discrete regions of either electrode materials or pores using segmentation algorithms [50]. Figures 3(a) and (b) show examples of the resulting two-phase (solid-pore) segmented image stacks for DIT and IIT electrodes, respectively. The measured width of the micro-pores was $4\text{--}7 \mu\text{m}$ for the DIT electrode, and $1\text{--}7 \mu\text{m}$ for the IIT electrode,

in agreement with the cross-sectional SEM images in Figure 2.

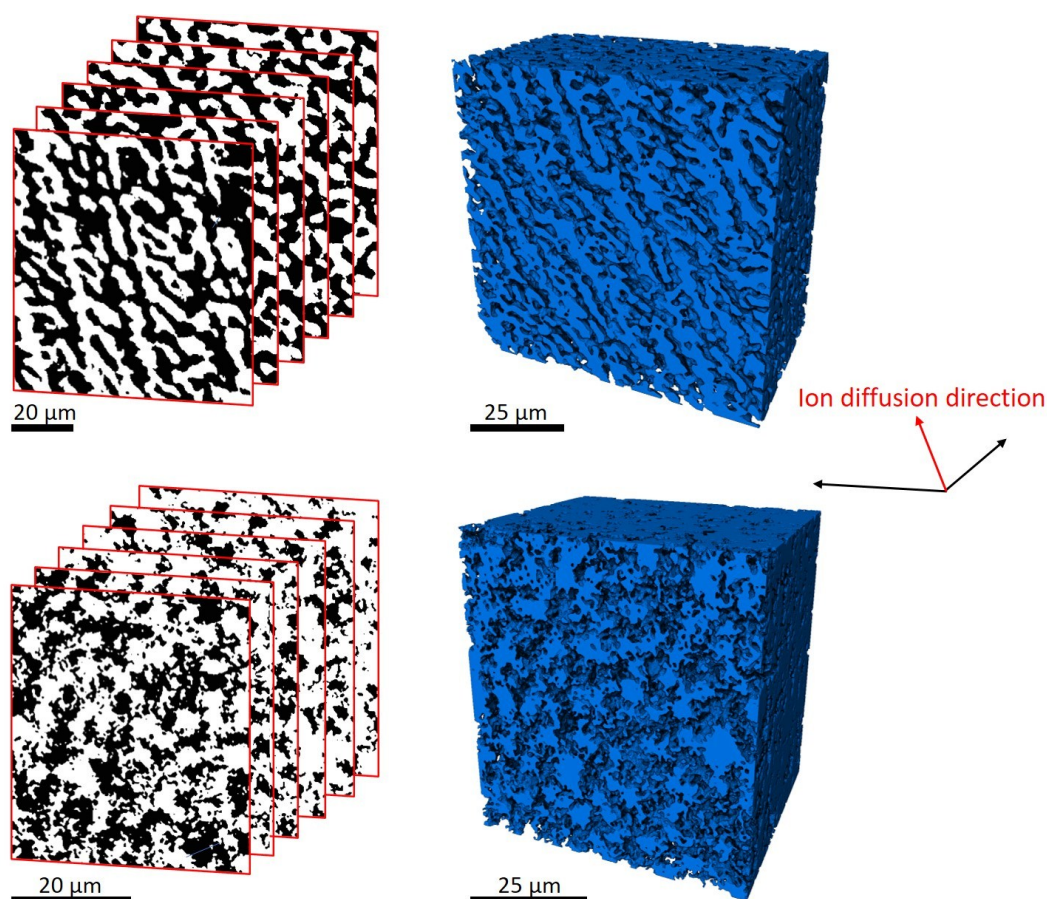


Figure 3: Representations of stacked 2D image slices after segmentation, showing the two-phase volumes of electrode structures made by (a) DIT; and (b) IIT (white is electrode material and black is pores). 3D rendering of electrode structures made by (c) DIT; and (d) IIT.

Porosity fraction ε was estimated by summing the voxels of the pore phase divided by the total volume, and was 36% and 44% for the IIT and DIT electrodes respectively. The differences in porosity fraction may relate to a more compact packing of the particles in the isotropic ice crystal network during IIT. The measured porosity fraction was consistent with that of other directionally porous cathodes e.g. 40-42% porosity for the LCO cathode made by magnetic templating [2], 44-57% porosity for the LCO cathode made by wood template [11] and 30-50% porosity for the NCA cathode made by ice templating [48]. The measured porosity fraction for the DIT electrode was also similar to the estimated 49%

porosity for commercial $\text{LiNi}_{0.3}\text{Mn}_{0.3}\text{Co}_{0.3}\text{O}_2$ (MNC) cathodes [51] and 37-41% for commercial LiFePO_4 electrodes [30], both made by SC.

Directional pore tortuosity τ was estimated using the open source MatLab application *TauFactor* [50], by comparing the lithium ion diffusive flux through the actual pore network (F_p) with that through an open volume of the same size (F_{cv}), in the through electrode thickness direction, according to [50]:

$$F_p = -AD \frac{\varepsilon}{\tau} \frac{\Delta C}{L} \quad (1)$$

$$F_{cv} = -AD \frac{\Delta C}{L} \quad (2)$$

where D is diffusivity of lithium ions in the electrolyte, $\Delta C=1$ is the arbitrary assumed difference in lithium ion concentration across an electrode thickness L with a cross-sectional area A . The 3D pore fraction from the tomography data was sub-divided into smaller sub-domains, and finite difference method-based simulations were used to calculate lithium ion transport through the 3D pore structure due to the assumed lithium ion concentration gradient. From those simulations, F_p and F_{cv} were obtained and taking the ratio of Equations 1 and 2 and rearranging yields the directional tortuosity $\tau = \varepsilon \frac{F_{cv}}{F_p}$ where $\tau=1$ represents idealized straight ion flux paths in one direction [50]. τ was estimated as 1.7 and 4.4 through the thickness of the DIT and IIT electrodes respectively for broadly similar overall porosity fractions. The directional tortuosity of the DIT electrode was also lower than $\tau \approx 3.2$ for commercial SC electrodes with a similar porosity of 41% [30].

Figure 3(c) shows a 3D rendering of the DIT electrode tomography data with pronounced aligned porosity consistent with the calculated low directional tortuosity. Supplementary Video 2 shows the

3D aligned porosity structure of the DIT electrode by XCT in more detail. Figure 3(d) shows a 3D rendering of the IIT electrode with a more random pore structure.

Electrochemical properties

Figure 4(a) shows the galvanostatic (dis)charge profiles of the DIT, IIT and SC electrodes at 0.1 C at the first cycle in a half cell configuration (C rate is defined as $1/n$ where n is the time in hours for complete charge or discharge at a given current). The reversible gravimetric capacity of the 900 μm thick DIT electrode at discharge was 142 mAh g^{-1} based on the mass of active material and competitive with the gravimetric capacity of the much thinner 26 μm SC electrode; in contrast, the randomly structured 900 μm thick IIT electrode had the lowest reversible gravimetric capacity of 76 mAh g^{-1} . For reference, the reversible capacity of LCO is usually $\sim 140 \text{ mAh g}^{-1}$ between 3 and 4.2 V in the literature [2, 4, 52, 53], corresponding to extracting and inserting approximately 0.5 Li per LiCoO_2 , if all of the active material has a sufficient supply of lithium ions. The Coulombic efficiency was 94%, 94% and 93% for the first cycle, and increased to 97%, 95% and 97% from the second cycle onwards for the DIT, IIT and SC electrodes, respectively.

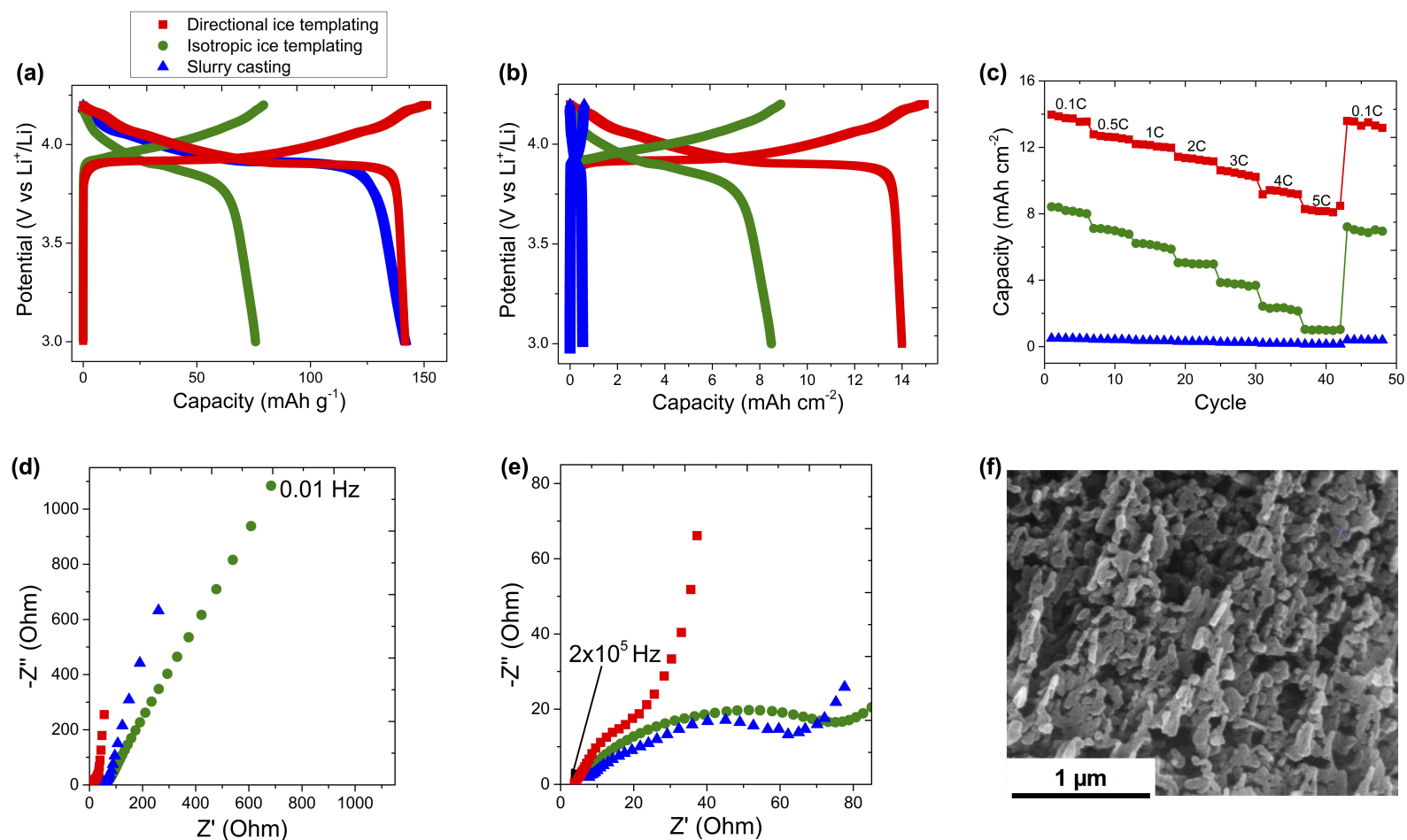


Figure 4: Charge and discharge profiles at 0.1 C for the LCO electrodes made by DIT, IIT and SC, showing (a) gravimetric capacities; and (b) corresponding areal capacities. (c) Reversible areal capacities of the three types of electrode at different C rates. (d) A Nyquist plot of the three types of electrode after 2 charge and discharge cycles in the frequency range 0.01 - 2×10^5 Hz at an open circuit potential, where the high frequency region is magnified in (e). (f) High-resolution cross-sectional SEM image of the surface of the LCO aligned pillar in the DIT electrode.

Figure 4(b) shows that the reversible areal capacities of the IIT and SC electrodes at 0.1 C were 8.4 and 0.5 mAh cm⁻² respectively. LCO electrodes made by SC exhibit areal capacities of 0.5 - 6 mAh cm⁻² at 0.1 C, where electrode thicknesses and densities vary [54]. The DIT electrode exhibited a higher reversible areal capacity of 14 mAh cm⁻². To investigate the effect of electrode structure on rate capability, Figure 4(c) shows the electrode reversible areal capacities at different C rates. The SC electrode capacity reduced by 72% from 0.1 to 5 C, and was typical of SC electrode performance e.g. [55, 57]. The IIT electrode capacity similarly reduced by 88% over the same range. The large capacity reduction was due to the increasingly restricted lithium ion diffusion in the random electrode structure at fast (dis)charge rates that starved some active regions of the electrode of lithium ions and reduced capacity significantly [8]. The DIT electrode capacity reduced by only 41% over the same range because the aligned micro-pores through the electrode thickness sustained effective lithium ion transport kinetics, competitive with the highest rate capability of LCO cathodes made by SC reported in the literature [55]. Figure S7 in the SI shows the reversible gravimetric capacities for the same types of electrode over the same C rate range, showing that the DIT electrode again sustained gravimetric capacity better than the IIT and SC electrodes. The volumetric capacities of the DIT, IIT and SC electrodes at 5 C were estimated as 92, 11 and 53 mAh cm⁻³ respectively, showing that the thick, open structured DIT electrode outperformed the thinner, compact SC electrode in volumetric capacity terms at the higher C rate.

Electrochemical impedance spectroscopy (EIS) was used to analyze ion diffusion kinetics in the three electrodes in a half-cell configuration after 2 charge and discharge cycles. Figure 4(d) shows the resulting Nyquist plot with the high frequency region magnified in Figure 4(e). An equivalent circuit for these Nyquist plot is shown in Figure S8 in the SI to understand individual resistance components [25]. The combined electrical resistance of the electrode and ionic resistance of the electrolyte R_s was estimated from the intercept of a best-fit to the Nyquist plot with the Z' axis at the highest frequency as 3.8,

7.1 and 7.3 Ω for the DIT, SC and IIT electrodes, respectively. The lowest R_s for the DIT electrode suggested that the coral-like electrode structure provided good electrical connectivity throughout the electrode, despite its thickness. As is common, the high frequency and medium-high frequency semi-circles could not be clearly separated [56]. The combined electrode/electrolyte interfacial resistance and charge transfer resistance of the electrode R_{CT} was estimated from the diameter of the more easily resolved semi-circle at medium-high frequency as 30, 61 and 77 Ω for the DIT, SC and IIT electrodes, respectively. The lower R_{CT} and the higher gradient of the Nyquist tail at the lowest frequencies for the DIT electrode confirmed faster lithium ion diffusion along the aligned porosity structure [56, 57], consistent with the lower measured directional pore tortuosity.

The comparatively low value of R_{CT} for the DIT electrode may indicate a relatively low electrode/electrolyte interfacial resistance [56]. Figure 4(f) is a magnified cross-sectional SEM image of the surface of the aligned pillar in the DIT electrode showing significant sub-micron porosity. If the electrode had experienced high temperature sintering as used elsewhere [2, 24–26], this fine-scale porosity can be expected to be reduced. Here, these sub-micron pores allowed lateral diffusion of lithium ions from the wide through-thickness pores into the finer coral-like electrode structure, and promoted a relatively high contact area between the active material and the electrolyte [58, 59]. The cyclic reversible capacity at 1 C for the DIT electrode is shown in Figure S9 in the SI, with a relatively high capacity retention of 90% after 200 cycles. The high capacity retention over cycling of the DIT electrode was again due to the aligned porosity structure, the comparatively high mechanical integrity, and the combination of micro- and nano-scale porosity that helped to buffer intercalation strains.

Performance and cost

Using the preceding data, the gravimetric and volumetric energy and power densities for both an LIB cell unit comprising a thick DIT LCO cathode, a separator, a lithium counter electrode and current collectors, and a stack of LIB cell units comprising commercial SC LCO cathodes, separators, lithium counter electrodes and current collectors, but of same total volume, were estimated. In order to provide a comparison between the DIT electrode and commercial SC electrodes, a thickness of 80 μm and a density of 2.1 g cm^{-3} were used that represent commercial electrodes [44, 51]. The thicknesses and densities of the inactive components (e.g. separators and current collectors) used in the estimation are listed in the SI, and are also consistent with commercial LIBs [44, 51]. The method of estimating energy and power densities is shown in the SI. The estimated vol.% and wt.% inactive components in the two types of LIB cell unit(s) of the same total volume are shown in Table S1 in the SI. The volumetric and gravimetric power densities for the two types of LIB cell unit(s) are shown in Table S2 in the SI. The estimated energy densities are for comparative purposes only and do not reflect the practically attainable energy densities of battery full cells because practical anodes with matching capacity and long cyclability would be required [44].

The energy densities at 1 C were 435 Wh kg^{-1} (509 Wh L^{-1}) for a DIT LCO/Li cell, compared with 308 Wh kg^{-1} (475 Wh L^{-1}) for a stack of SC LCO/Li cells of the same total volume. The estimated energy densities at 2 C were 408 Wh kg^{-1} (477 Wh L^{-1}) for the DIT LCO/Li cell, higher than 260 Wh kg^{-1} (402 Wh L^{-1}) for the stack of SC LCO/Li cells of the same volume, where rates of 1-2 C approximate to a typical drive-cycle test for an electric vehicle [2]. The volumetric energy density of the DIT LCO cell was higher than 400-420 Wh L^{-1} , which is typical for commercially available prismatic and cylindrical LIB technologies using calendered SC electrodes at low C rates of 0.05 - 0.5 C [60]. The

volumetric energy density of LCO LIB cells usually decreases by $\sim 20\%$ from 0.1 to 1 C, and decreases by $\sim 30\%$ from 0.1 to 2 C due to restricted ion diffusion kinetics [55], whereas the volumetric energy density of the DIT LCO-based cell decreased by $\sim 10\%$ from 0.1 to 1 C, and $\sim 20\%$ from 0.1 to 2 C, demonstrating the higher rate capability for the DIT electrodes. Even though the thick DIT electrodes have a relatively higher overall pore fraction than calendered SC electrodes, they deliver a high energy density and rate capability due to a lower proportion of inactive components per unit cell volume and faster ion transport along the aligned micro-pores at increasing C rates.

A cost analysis was also performed to assess economic feasibility of the DIT technique. The costs of the active components, inactive components and electrode processing steps for the DIT LCO cell and the SC LCO cell-stack of the same total volume are listed in Table S3 in the SI. The costs associated with the SC LCO cell-stack are consistent with commercial LIBs [51]. The DIT LCO cell reduced the cost of active components by $36\% \text{ kWh}^{-1}$ at 2 C, reduced the cost of inactive components by $\sim 60\%$, reduced the cost of solvent used in electrode processing by 99% and eliminated the solvent recovery step compared with making an SC cell-stack. However, since the DIT technique requires freezing water and ice sublimation, associated costs and to a first level of approximation, were at estimated ~ 7 times higher than slurry coating and drying SC electrodes. Overall a DIT LCO cell could be approximately cost competitive with an SC LCO cell.

Conclusions

Ultra-thick ($900 \mu\text{m}$) coral-like, aligned porosity LCO LIB cathodes were fabricated by DIT without any post-processing sintering. Using XCT and electrochemical impedance spectroscopy, the low directional

pore tortuosity of the DIT electrodes was directly related to their improved lithium ion transport in the through-thickness direction when compared with the IIT and SC electrodes of the same composition. Of the three types of electrodes, the DIT electrodes exhibited the highest areal and gravimetric capacities, and sustained the highest rate capability because: (i) the inter-connected LCO structure provided good electrical connectivity throughout the electrode, despite its thickness; (ii) the aligned micro-pores through the electrode thickness promoted fast lithium ion transport in the predominant lithium ion diffusion direction; and (iii) the avoidance of sintering retained sub-micron pores that promoted a relatively high electrode/electrolyte interfacial area and efficient lithium (de)intercalation reactions. These results suggest a promising approach to the challenge of ultra-thick electrode designs for increasing capacity while retaining useful rate capability.

Experimental

Electrode fabrication

Suspensions were prepared by mixing LCO particles (Sigma Aldrich), Super P carbon black (Alfa Aesar) and sodium carboxymethyl cellulose (CMC, Sigma Aldrich) binder at a weight ratio of 25 : 1 : 1, and dispersing homogeneously by sonication in deionised water. For making electrodes by DIT, the electrodes were made by directionally freezing the suspension in a custom-made 3D printed acrylonitrile butadiene styrene (ABS) mould on polished copper plates. Upon freezing, the suspension was cooled from room temperature to 193 K at 0.1 and 0.5 K s⁻¹ until fully solid. After demoulding, the free-standing frozen electrodes were immediately freeze dried at 220 K and 0.014 mBar for 15 h to sublime ice from the electrodes. For making electrodes by IIT, the electrodes were made by freezing the suspension from all directions. The freeze drying method for preparing electrode materials has also been reported in [61,62].

For making electrodes by SC, since suspending cathode materials of lithium oxides (LCO, $\text{LiNi}_{1/3}\text{Mn}_{1/3}\text{Co}_{1/3}\text{O}_2$, LiNiCoAlO_2 , etc.) in water rather than an organic solvent such as N-methyl-pyrrolidone (NMP) increases the pH of the slurries [63], the Al_2O_3 passive film always present on Al current collectors usually used for the lithium oxides cathodes becomes soluble in the high pH conditions, and the Al underneath becomes sensitive to side reactions when in contact with the alkaline aqueous cathode slurries [64–66]. Therefore, because an aqueous slurry was used here for SC to allow direct performance comparison with the ice templated electrodes, stainless steel (type 304, average thickness 28 μm , similar thickness to the standard Al foils) current collectors were used to prevent any side reactions of the current collectors; stainless steel current collectors have also been reported previously for similar testing [67]. Although Al has a higher electrical conductivity than stainless steel, the electrical conductivity of both Al and stainless steel is orders of magnitude higher than that of the electrodes, and switching the current collector from Al to stainless steel did not influence the electrochemical characterization of the electrodes [63]. The SC electrodes on Al foil current collectors were later tested and exhibited similar capacities. The SC electrodes underwent the same drying process as the ice templated electrodes to provide a fair comparison in performance.

Characterization

The electrode weight was measured by a microbalance (Sartorius) with 0.01 mg accuracy. Compression of the free-standing electrodes was performed by a Shimadzu mechanical testing machine. Stress σ was estimated from $\sigma = F/A_0$ and strain ε was estimated from $\varepsilon = \delta/L_0$, where F is the load, A_0 is the original sample cross-sectional area, δ is the axial displacement and L_0 is the original sample thickness

(=900 μm).

The electrodes before and after cycling were investigated by X-ray diffraction (XRD, Siemens D5000) with a Cu_α radiation $\lambda=1.5 \text{ \AA}$. The morphology of the electrodes was examined by SEM (JEOL 6500F). Cross-sections of the electrodes were prepared by a Gatan Precision Etching Coating System (PECS 685) at 6 kV beam for 2 hr. XCT was performed by Zeiss Xradia 510 and segmented by software Avizo. The resulting binarized reconstruction was cropped to the largest possible volume of $360 \times 665 \times 305$ voxels, corresponding to a total volume of $5.8 \times 10^5 \mu\text{m}^3$. The total number of 2D image slices for each sample was 2613. Electrical conductivity of the 900 μm thick, self-standing DIT electrodes was measured by using a current source (Keithley 220 Programmable Current Source) and a nano-volt meter (Agilent 34420A nano-volt/micro-ohm meter) in a standard four-point probe configuration. The testing samples were selected from 5 batches, measurements were performed at 3 different locations on each sample, and repeated 6 times for each location. The standard SC electrodes were tested in standard CR2032 coin cells. Due to the ultra-high thickness of the ice templated electrodes, the ice templated electrodes were tested in standard Swagelok cells, all in the same half-cell configuration. All cells were assembled in a glovebox. Lithium foil was used as the counter electrode, and 1 M LiPF_6 dissolved in a mixed solvent of ethylene carbonate (EC) and diethyl carbonate (DEC) in 1:1 v/v was used as the electrolyte. The cells were galvanostatically charged (lithiation) from 3 V to 4.2 V vs. Li/Li^+ at 0.1 C and then discharged at different C rates at room temperature using battery cyclers (Arbin BT-G-25). Electrochemical impedance spectroscopy was performed in the $2 \times 10^5 - 0.01$ Hz frequency range at room temperature using Reference 600/EIS300 Gamry potentiostat/galvanostat. 60 cells from different templating experiments were measured to verify reproducibility of capacities, which was estimated as $\pm 4\%$.

Acknowledgments

This work was partly supported by the UK Engineering and Physical Sciences Research Council (EPSRC) through Grant EP/M009521/1 - "Enabling Next Generation Li-ion Batteries". The use of facilities funded by EPSRC Grant EP/M02833X/1 University of Oxford: experimental equipment upgrade is gratefully acknowledged. The author would like to thank Prof Peter G. Bruce for the precision etching and coating system (PECS) sample preparation, Prof Mauro Pasta for the glovebox, Prof Nigel Brandon and Dr Samuel J. Cooper for helpful discussions with the Tau Factor, and Prof Richard I. Todd and Mr Thomas Scott for access to mechanical testing.

Competing financial interests statement

The author(s) declare no competing financial interests.

References

- [1] J. M. Tarascon and M. Armand, Issues and challenges facing rechargeable lithium batteries, *Nature* 414 (2001) 359-367.
- [2] J. S. Sander, R. M. Erb, L. Li, A. Gurijala and Y.-M. Chiang, High-performance battery electrodes via magnetic templating, *Nat. Energy* 1 (2016) 1-7.
- [3] D. Gordon, M. Y. Wu, A. Ramanujapuram, J. Benson, J. T. Lee, A. Magasinski, N. Nitta, C. Huang, G. Yushin, Enhancing cycle stability of lithium iron phosphate in aqueous electrolytes by increasing electrolyte molarity, *Adv. Energy Mater.* 6 (2016) 1501805.

- [4] H. Zheng, J. Li, X. Song, G. Liu and V. S. Battaglia, A comprehensive understanding of electrode thickness effects on the electrochemical performances of Li-ion battery cathodes, *Electrochim. Acta* 71 (2012) 258-265.
- [5] A. Kraytsberg and Y. Ein-Eli, Conveying Advanced Li-ion Battery Materials into Practice, The Impact of Electrode Slurry Preparation Skills, *Adv. Energy Mater.* 6 (2016) 1600655.
- [6] M. Ebner, D.-W. Chung, R. E. Garcia and V. Wood, Tortuosity anisotropy in lithium-ion battery electrodes, *Adv. Energy Mater.* 4 (2014) 1301278.
- [7] J. Newman and K. E. Thomas-Alyea, *Electrochemical Systems*, John Wiley & Sons, Inc, 2004.
- [8] M. Doyle and J. Newman, Analysis of capacity-rate data for lithium batteries using simplified models of the discharge process, *J. Appl. Electrochem.* 27 (7) (1997) 846-856.
- [9] N. Balke, S. Jesse, A. N. Morozovska, E. Eliseev, D. W. Chung, Y. Kim, L. Adamczyk, R. E. Garcia, N. Dudney and S. V. Kalinin, Nanoscale mapping of ion diffusion in a lithium-ion battery cathode, *Nature Nanotechnology* 5 (2010) 749754.
- [10] Y.-H. Chen, C.-W. Wang, X. Zhang, X. and A. M. Sastry, Porous cathode optimization for lithium cells: ionic and electronic conductivity, capacity, and selection of materials, *J. Power Sources*. 195 (2010) 2851-2862.
- [11] L.-L. Lu, Y.-Y. Lu, Z.-J. Xiao, T.-W. Zhang, F. Zhou, T. Ma, Y. Ni, H.-B. Yao, S.-H. Yu, Y. Cui, Wood-inspired high-performance ultrathick bulk battery electrodes, *Adv. Mater.* 1706745 (2018) 1-9.
- [12] S. Oro, K. Urita and I. Moriguchi, Nanospace-controlled SnO₂/nanoporous carbon composite as a high-performance anode for sodium ion batteries, *Chem. Lett.* 46 (2017) 502-505.

- [13] S. Oro, K. Urita and I. Moriguchi, Nanospace control of SnO₂ nanocrystallites-embedded nanoporous carbon for reversible electrochemical chargedischarge reactions, *J. Phys. Chem. C* 120 (2016) 2571725724.
- [14] Y. Zhang, Y. Lu, S. Feng, D. Liu, Z. Ma and S. Wang, On-site evolution of ultrafine ZnO nanoparticles from hollow metalorganic frameworks for advanced lithium ion battery anodes, *J. Mater. Chem. A* 5 (2017) 22512-22518.
- [15] H. Liu, L. Tao, Y. Zhang, C. Xie, P. Zhou, H. Liu, R. Chen and S. Wang, Bridging covalently functionalized black phosphorus on graphene for high-performance sodium-ion battery, *ACS Appl. Mater. Interfaces* 9 (42) (2017) 36849-36856.
- [16] H. Liu, Y. Zou, L. Tao, Z. Ma, D. Liu, P. Zhou, H. Liu and S. Wang, Sandwiched thin-film anode of chemically bonded black phosphorus/graphene hybrid for lithium-ion battery, *Small* 13 (2017) 1700758.
- [17] Z. Ma, L. Tao, D. Liu, Z. Li, Y. Zhang, Z. Liu, H. Liu, R. Chen, J. Huo and S. Wang, Ultrafine nano-sulfur particles anchored on in situ exfoliated graphene for lithiumsulfur batteries, *J. Mater. Chem. A* 5 (2017) 9412-9417.
- [18] Z. Li, H. B. Wu and X. W. D. Lou, Rational designs and engineering of hollow micro-/nanostructures as sulfur hosts for advanced lithiumsulfur batteries, *Energy Environ. Sci.* 9 (2016) 3061-3070.
- [19] S. L. Zhang, B. Y. Guan, H. B. Wu and X. W. D. Lou, Metalorganic framework-assisted synthesis of compact Fe₂O₃ nanotubes in Co₃O₄ host with enhanced lithium storage properties, *Nano-Micro Lett.* 10 (2018) 44.

- [20] Y. Lu, J. Nai, X. W. D. Lou, Formation of $\text{NiCo}_2\text{V}_2\text{O}_8$ yolkdouble shell spheres with enhanced lithium storage properties, *Angew. Chem. Int. Ed* 57 (2018) 2899-2903.
- [21] Y. Lu, L. Yu, M. Wu, Y. Wang and X. W. D. Lou, Construction of complex $\text{Co}_3\text{O}_4@\text{Co}_3\text{V}_2\text{O}_8$ hollow structures from metalorganic frameworks with enhanced lithium storage properties, *Adv. Mater.* 30 (2018) 1702875.
- [22] C. Huang, N. P. Young, J. Zhang, H. J. Snaith and P. S. Grant, A two layer electrode structure for improved Li ion diffusion and volumetric capacity in Li ion batteries, *Nano Energy* 31 (2017) 377-385.
- [23] P. Pietsch, D. Westhoff, J. Feinauer, J. Eller, F. Marone, M. Stampanoni, V. Schmidt and V. Wood, Quantifying microstructural dynamics and electrochemical activity of graphite and silicon-graphite lithium ion battery anodes, *Nature Communications* 7 (2016) 12909.
- [24] C.-J. Bae, C. K. Erdonmez, J. W. Halloran and Y.-M. Chiang, Design of battery electrodes with dual-scale porosity to minimize tortuosity and maximize performance, *Adv. Mater.* 25 (2013) 1254-1258.
- [25] C. Chen, Y. Zhang, Y. Li, Y. Kuang, J. Song, W. Luo, Y. Wang, Y. Yao, G. Pastel, J. Xie and L. Hu, Highly conductive, lightweight, low-tortuosity carbon frameworks as ultrathick 3D current collectors, *Adv. Energy Mater.* 7 (2017) 1700595.
- [26] S. Behr, R. Amin, Y. M. Chiang and A. P. Tomsia, Highly structured, additive free lithium-ion cathodes by freeze-casting technology, *Ceram. Forum Int.* 92 (2015) E39-E43.
- [27] S. Deville, E. Saiz, R. K. Nalla and A. P. Tomsia, Freezing as a path to build complex composites, *Science* 311 (2006) 515-518.

- [28] G. Bucci, T. Swamy, S. Bishop, B. W. Sheldon, Y.-M. Chiang and W. C. Cartera, The effect of stress on battery-electrode capacity, *J. Electrochem. Soc.* 164 (4) (2017) A645-A654.
- [29] H. Moriwake, A. Kuwabara, C. A. J. Fisher, R. Huang, T. Hitosugi, Y. H. Ikuhara, H. Oki and Y. Ikuhara, First-principles calculations of lithium-ion migration at a coherent grain boundary in a cathode material, LCO, *Adv. Mater.* 25 (2013) 618-622.
- [30] S. J. Cooper, D. S. Eastwood, J. Gelb, G. Damblanc, D. J. L. Brett, R. S. Bradley, P. J. Withers, P. D. Lee, A. J. Marquis, N. P. Brandon and P. R. Shearing, Image based modelling of microstructural heterogeneity in LiFePO_4 electrodes for Li-ion batteries, *J. Power Sources* 247 (2014) 1033-9.
- [31] D. A. G. Bruggeman, Berechnung verschiedener physikalischer Konstanten von heterogenen Substanzen. I. Dielektrizitätskonstanten und Leitfähigkeiten der Mischkörper aus isotropen Substanzen. *Ann. Phys.* 416 (7) (1935) 969-664.
- [32] A. C. Forse, J. M. Griffin, C. Merlet, J. Carretero-Gonzalez, A.-R. O. Raji, N. M. Trease and C. P. Grey, Direct observation of ion dynamics in supercapacitor electrodes using in situ diffusion NMR spectroscopy, *Nat. Power* 2 (2017) 16216.
- [33] O. Pecher, J. Carretero-Gonzalez, K. J. Griffith and C. P. Grey, Materials methods: NMR in battery research, *Chem. Mater.* 29 (2017) 213-242.
- [34] C.-C. Li, Y.-W. Wang, Importance of binder compositions to the dispersion and electrochemical properties of water-based LiCoO_2 cathodes, *J. Power Sources* 227 (2013) 204-210.
- [35] S.-L. Chou, J.-Z. Wang, H.-K. Liu, S.-X. Dou, Rapid synthesis of $\text{Li}_4\text{Ti}_5\text{O}_{12}$ microspheres as anode materials and its binder effect for lithium-ion battery, *J. Phys. Chem. C* 115 (2011) 16220-16227.

- [36] J.-S. S. Bridel, T. Azais, M. Morcrette, J.-M. M. Tarascon and D. Larcher, Key parameters governing the reversibility of Si/carbon/CMC electrodes for Li-ion batteries, *Chem. Mater.* 22 (3) (2010) 1229-1241.
- [37] S. Deville, E. Maire, G. Bernard-Granger, A. Lasalle, A. Bogner, C. Gauthier, J. Leloup and C. Guizard, Metastable and unstable cellular solidification of colloidal suspensions, *Nat. Mater.* 8 (2009) 966-972.
- [38] K. Kierzek, J. Machnikowaski and F. Beguin, Towards the realistic silicon/carbon composite for Li-ion secondary battery anode, *J. Appl. Electrochem.* 45 (2015) 1-10.
- [39] M. Singh, J. Kaiser and H. Hahna, Thick electrodes for high energy lithium ion batteries, *J. Electrochem. Soc.* 162 (7) (2015) A1196-A1201.
- [40] K. Evanoff, J. Khan, J. A. A. Balandin, A. Magasinski, W. J. Ready, T. F. Fuller and G. Yushin, Towards ultrathick battery electrodes: aligned carbon nanotube-enabled architecture, *Adv. Mater.* 24 (4) (2012) 533-7.
- [41] S. W. Sofie, Fabrication of functionally graded and aligned porosity in thin ceramic substrates with the novel freeze-tape-casting process, *J. Am. Ceram. Soc.* 90 (7) (2007) 2024-2031.
- [42] Y. Liu, X.-Y. Yu, and Y. Fang, X. Zhu, J. Bao, X. Zhou and X. W. D. Lou, Conning SnS₂ ultrathin nanosheets in hollow carbon nanostructures for efficient capacitive sodium storage, *Joule* 2 (2018) 725-735.
- [43] Y. Yang, X. Li, M. Wen, E. Hacıopian, W. Chen, Y. Gong, J. Zhang, B. Li, W. Zhou, P. M. Ajayan, Q. Chen, T. Zhu and J. Lou, Brittle fracture of 2D MoSe₂, *Adv. Mater.* 29 (2017) 1604201.

- [44] F. Wu and G. Yushin, Conversion cathodes for rechargeable lithium and lithium-ion batteries, *Energy Environ. Sci.* 10 (2017) 435-459.
- [45] E. Munch, M. E. Launey, D. H. Alsem, E. Saiz, A. P. Tomsia and R. O. Ritchie, Tough, bio-inspired hybrid materials, *Science* 322 (2008) 1516-1520.
- [46] J. Seuba, S. Deville, C. Guizard and A. J. Stevenson, Mechanical properties and failure behavior of unidirectional porous ceramics, *Sci. Reports* 6:24326 (2016) DOI: 10.1038/srep24326.
- [47] C. Huang, N. Grobert, A. A. R. Watt, C. Johnston, A. Crossley, N. P. Young and P. S. Grant, Layer-by-layer spray deposition and unzipping of single-wall carbon nanotube-based thin film electrodes for electrochemical capacitors, *Carbon* 61 (2013) 525-536.
- [48] B. Delattre, R. Amin, J. Sander, J. D. Coninck, A. P. Tomsia, Y.-M. Chiang, Impact of pore tortuosity on electrode kinetics in lithium battery electrodes: study in directionally freeze-cast $\text{LiNi}_{0.8}\text{Co}_{0.15}\text{Al}_{0.05}\text{O}_2$ (NCA), *J. Electrochem. Soc.* 165, 2 (2018) A388-A395.
- [49] F. A. L. Dullien, *Porous Media: Fluid Transport and Pore Structure*, Academic Press, San Diego, 1992.
- [50] S. J. Cooper, A. Bertei, P. R. Shearing, J. A. Kilner and N. P. Brandon, TauFactor: An open-source application for calculating tortuosity factors from tomographic data, *Software X* 5 (2016) 203-210.
- [51] D. L. Wood III, J. Li, C. Daniel, Prospects for reducing the processing cost of lithium ion batteries, *J. Power Sources* 275 (2015) 234-242.
- [52] A. Ramanujapuram, D. Gordon, A. Magasinski, B. Ward, N. Nitta, C. Huang and G. Yushin, Degradation and stabilization of lithium cobalt oxide in aqueous electrolytes, *Energy Environ. Sci.* 9 (2016) 1841-1848.

- [53] T. Ohzuku and A. Ueda, Why transition metal (di)oxides are the most attractive materials for batteries, *Solid State Ionics* 69 (1994) 201-211.
- [54] E. C. Self, E. C. McRen, R. Wycisk, P. N. Pintauro, LiCoO₂-based fiber cathodes for electrospun full cell Li-ion batteries, *Electrochim. Acta* 214 (2016) 139-146.
- [55] S. Kalluri, M. Yoon, M. Jo, S. Park, S. Myeong, J. Kim, S. Dou, Z. Guo, J. Cho, Surface engineering strategies of layered LiCoO₂ cathode material to realize high-energy and high-voltage Li-ion cells, *Adv. Energy Mater.* 7 (2017) 1601507.
- [56] N. Schweikert, R. Heinzmann, A. Eichhfer, H. Hahn and S. Indris, Electrochemical impedance spectroscopy of Li₄Ti₅O₁₂ and LiCoO₂ based half-cells and Li₄Ti₅O₁₂/LiCoO₂ cells: Internal interfaces and influence of state-of-charge and cycle number, *Solid State Ionics* 226 (2012) 15-23.
- [57] B. Shen, P. Zuo, P. Fan, J. Yang, G. Yin, Y. Ma, X. Cheng, C. Du, Y. Gao, Improved electrochemical performance of NaAlO₂-coated LiCoO₂ for lithium-ion batteries, *J. Solid State Electrochem.* 21 (2017) 11951201.
- [58] Y.-S. Hu, P. Adelhelm, B. M. Smarsly, S. Hore, M. Antonietti and J. Maier, Synthesis of hierarchically porous carbon monoliths with highly ordered microstructure and their application in rechargeable lithium batteries with high-rate capability, *Adv. Funct. Mater.* 17 (2007) 1873-1878.
- [59] Y.-G. Guo, Y.-S. Hu, W. Sigle and J. Maier, Superior electrode performance of nanostructured mesoporous TiO₂ (anatase) through efficient hierarchical mixed conducting networks, *Adv. Mater.* 19 (2007) 2087-2091.
- [60] W. Lai, C. K. Erdonmez, T. F. Marinis, C. K. Bjune, N. J. Dudney, F. Xu, R. Wartena, Y.-M. Chiang, Ultrahigh-energy-density microbatteries enabled by new electrode architecture and micropackaging design, *Adv. Energy Mater.* 22 (2010) E139-E144.

- [61] F. Tu, X. Xu, P. Wang, L. Si, X. Zhou, J. Bao, Jianchun, A few-layer SnS₂/reduced graphene oxide sandwich hybrid for efficient sodium storage, *J. Phys. Chem. C* 121 (2017) 3261-3269.
- [62] Y. Du, X. Zhu, X. Zhou, L. Hu, Z. Dai, J. Bao, Co₃S₄ porous nanosheets embedded in graphene sheets as high-performance anode materials for lithium and sodium storage, *J. Mater. Chem. A* 3 (2015) 6787-6791.
- [63] S. Y. Li and B. C. Church, Effect of aqueous-based cathode slurry pH and immersion time on corrosion of aluminum current collector in lithium-ion batteries, *Mater. Corros.* 67 (9) (2016) 978-987.
- [64] B. Zaid, D. Saidi, A. Benzaid, S. Hadji, Effects of pH and chloride concentration on pitting corrosion of AA6061 aluminum alloy, *Corros. Sci.* 50 (2008) 1841-1847.
- [65] J. W. Braithwaite, A. Gonzales, G. Nagasubramanian, S. J. Lucero, D. E. Peebles, J. A. Ohlhausen and W. R. Cieslak, Corrosion of lithium-ion battery current collectors, *J. Electrochem. Soc.* 146 (2) (1999) 448-456.
- [66] B. C. Church, D. T. Kaminski and J. Jiang, Corrosion of aluminum electrodes in aqueous slurries for lithium-ion batteries, *J. Mater. Sci.* 49 (8) (2014) 3234-3241.
- [67] C. Huang, J. Zhang, H. J. Snaith and P. S. Grant, Engineering the membrane/electrode interface to improve the performance of solid-state supercapacitors, *ACS Appl. Mater. Interfaces* 8 (2016) 20756-20765.

Graphical abstract

